

Contents lists available at ScienceDirect

Petroleum Science

journal homepage: www.keaipublishing.com/en/journals/petroleum-science



Original Paper

Lacustrine organic carbon sequestration driven by volcanism: A case study of the third submember of the Chang 7 Member of the Yanchang Formation in the Ordos Basin



Jia-Hong Gao, Zhi-Jun Jin*, Xin-Ping Liang

State Key Laboratory of Shale Oil and Gas Enrichment Mechanisms and Efficient Development, Institute of Energy, Peking University, Beijing, 100871, China

ARTICLE INFO

Article history:
Received 8 October 2024
Received in revised form
31 March 2025
Accepted 19 May 2025
Available online 24 May 2025

Edited by Xi Zhang and Jie Hao

Keywords: Carbon burial rate Volcanism Organic-rich shale Paleoclimate Ordos Basin

ABSTRACT

The Ordos Basin was recognized as the earliest terrestrial aquatic ecosystem to recover following Permian-Triassic mass extinction, significantly contributing to organic carbon sequestration during the early Mesozoic era. Volcanic activity has increased the organic carbon burial capacity of the third submember of Ch7 (Ch7₃) within this basin, although it has both positive and negative effects on organic carbon burial. In this study, we quantitatively characterized the organic carbon burial process by calculating the organic carbon accumulation rate (OCAR) and proposed an optimal sedimentary model influenced by volcanic activity. We conducted time series analysis on gamma ray (GR) data from Ch7₃ to determine sedimentation rates (SRs) while measuring the density of each sample via hydrostatic methods. By integrating these measurements with the total organic carbon (TOC) content, we established a dynamic OCAR for Ch7₃ ($\bar{x} = 0.68 \text{ g/(cm}^2 \cdot \text{kyr})$) and estimated that it sequestered 0.27 Tt of organic carbon. Our findings indicate that the OCAR under eunixic conditions ($\bar{x} = 1.02 \text{ g/(cm}^2 \cdot \text{kyr})$) is 2.49 times greater than that under ferruginous conditions ($\bar{x} = 0.41 \text{ g/(cm}^2 \text{ kyr)}$). The geochemical identification fingerprints of volcanism suggest that the top of Ch73 is influenced by volcanoes of appropriate intensity. In this sedimentary model, the dilution of organic matter (OM) by rapidly deposited volcanic ash is relatively low. Additionally, the cumulative effect of chemical weathering intensity due to volcanic activity leads to the input of nutrients from continental sources into the lake basin. This process promotes increased productivity, resulting in a significant increase in the OCAR $(\bar{x} = 0.76 \text{ g/(cm}^2 \cdot \text{kyr}))$. This study provides new insights for dynamically assessing the impact of geological events on the OCAR.

© 2025 The Authors. Publishing services by Elsevier B.V. on behalf of KeAi Communications Co. Ltd. This is an open access article under the CC BY-NC-ND license (http://creativecommons.org/licenses/by-nc-nd/4.0/).

1. Introduction

Black shale is a distinctive stratigraphic layer characterized by its high organic content and typically forms under anoxic conditions. This sedimentary formation arises from the complex interactions of materials and energy within the Earth's layers, serving as a crucial medium for understanding geological changes (Tissot and Welte, 1984; Galvez et al., 2020; Liang et al., 2021; Jin et al., 2023). The formation and preservation of black shale are influenced by various factors, including biological activity, aquatic

E-mail address: jinzj1957@pku.edu.cn (Z.-J. Jin).

Peer review under the responsibility of China University of Petroleum (Beijing).

conditions, and sediment dynamics; it encapsulates significant geological and biological processes from its formation and is often enriched with valuable metals (Tissot and Welte, 1984; Jiang et al., 2025). In the petroleum industry, black shales with total organic carbon (TOC) contents exceeding 0.5 wt% are recognized as effective hydrocarbon source rocks (Tissot and Welte, 1984; Zhao et al., 2019; Gao et al., 2023; Cao et al., 2024). Understanding the complexities of Earth's changing systems and the mechanisms behind hydrocarbon and metal resource accumulation is essential. Furthermore, black shale offers critical insights into past environmental conditions and structural configurations.

Volcanic activity is intricately linked to biological extinction and evolution. Increases in biological mortality rates are often attributed to abrupt environmental changes, such as the eruptions of large igneous provinces (LIPs) (Algeo and Shen, 2023). These

 $[\]ast$ Corresponding author.

events can trigger stress responses that lead to morphologically observable abnormalities as well as mild genetic disturbances and deformations (Bos et al., 2024). Additionally, the supply of phosphorus (P) is typically more limited than that of nitrogen (N), which is accessible through autotrophic growth via photosynthesis (Walton et al., 2023; Wang et al., 2023). This limitation may hinder biological development in terrestrial river and lake ecosystems (Chen, 2023). Consequently, the substantial release of P associated with volcanic activity can significantly increase the efficiency of the N–P cycle within these ecosystems (Carrillo, 2021). While volcanic activity appears to have both positive and negative effects on organic matter (OM) sequestration, the optimal conditions for enhancing organic carbon sequestration capacity remain unclear.

Previous studies have indicated that the high concentrations of OM in the Chang 7 Member (Ch7) of the Ordos Basin are linked to volcanic activity (Liu et al., 2024). Volcanic influences were observed at the base of the third submember of Ch7 (Ch7₃) (Zhang et al., 2009), with increasing intensity and decreasing carbon isotope values (Chen et al., 2020). Following volcanic events, the OM content progressively increased. Notably, carbon isotope recovery occurred rapidly, underscoring the importance of organic carbon sequestration during recovery phases, which is likely driven by persistent anoxic conditions (Dal Corso et al., 2020; Sun et al., 2020; Lu et al., 2021; Tomimatsu et al., 2021). However, excessive volcanic ash can trigger bacterial sulfate reduction (BSR) and dilute OM, indicating that the degree of OM enrichment depends on initial paleoproductivity levels and OM preservation (Liu et al., 2021). This illustrates both the positive and negative aspects of organic carbon burial under volcanic activity in Ch7₃. However, the precise influence process of volcanism on OM burial processes remain unclear. We examine Ch73 of the Ordos Basin as a case study to determine the optimal organic carbon deposition model for lake basins influenced by volcanic activity, thereby providing a better foundation for selecting favorable intervals.

2. Geological setting

During the Middle to Late Triassic period, the North China Plate became part of the northeastern region of Pangea. The Ordos Basin, a large multicyclic cratonic basin covering approximately 320,000 km² (Yang et al., 2005), has been situated in the western part of the North China Plate since the late Permian. Throughout the Triassic, the basin was located at approximately 30 °N latitude, within a temperate-subtropical climate zone (Ji et al., 2010). Today, the Ordos Basin is bordered by the Yinshan Mountains to the north, the Qinling Orogenic Belt to the south, the Taihang Mountains to the east, and the Ordos Western Margin Thrust Belt to the west (Fig. 1). By the end of the Triassic, the basin had undergone a significant transition from marine to continental lacustrine sedimentation (Wu et al., 2023).

The Upper Triassic Yanchang Formation is characterized by a series of terrigenous clastic deposits derived from river-delta-lake systems (Wu et al., 2023). This formation is subdivided into ten submembers (Chang 1–Chang 10), which are identified by marker beds, sedimentary cycles, and lithological associations, collectively representing a notable Mesozoic petroleum system (Fig. 2). Ch7 is particularly significant and consists of siltstone, mudstone, organic-rich shale, and laminated volcanic ash layers, with total thicknesses ranging from 80 to 120 m. Recent studies of the Yanchang Formation, particularly Ch7, have revealed sedimentary features indicative of strong tectonic influences, including seismites, volcanic ash deposits, and distinctive mineral formations (e. g., pyrite veins, marcasite, gypsum, and manganese nodules) associated with hydrothermal fluid dynamics.

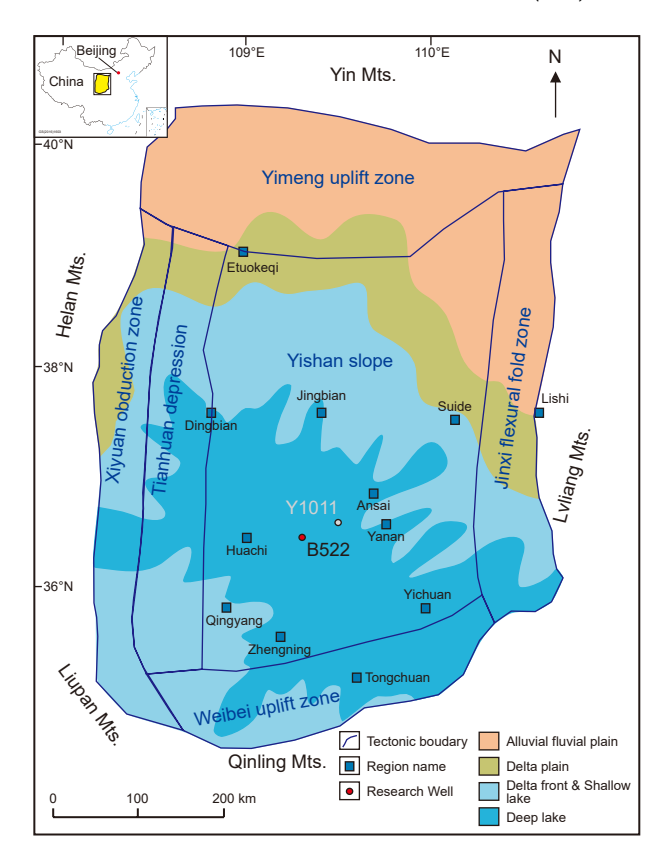


Fig. 1. Sedimentary facies distribution map of Ch7 in the Ordos Basin (Gao et al., 2023).

The lower section of $Ch7_3$ is primarily composed of a thick layer of black, organic-rich shale interspersed with tuff layers. In contrast, the upper section of $Ch7_3$ features dark gray shale interbedded with fine-grained sandstones and siltstones. The $Ch7_2$ and $Ch7_1$ members consist of dark gray shale interleaved with silty shale, siltstones, and fine-grained sandstones.

3. Samples and methods

The samples utilized in this study were sourced primarily from Well B522 in the Ordos Basin, which is located in the western region of the North China Craton (Fig. 1). The selected samples were gray, gray-black, and black shale. Following polishing, these samples were analyzed via optical microscopy (Fig. 2).

3.1. Total organic carbon (TOC)

For total organic carbon (TOC) analysis, sections of the samples were treated with 4.5% hydrochloric acid to remove inorganic carbon, while other portions were left untreated. The samples were subsequently incinerated at a high temperature of 1250 °C in an oxygen-rich environment to quantify the TOC. This analysis was performed via a Skyray CS-188 carbon-sulfur analyzer at the Laboratory of Organic Geochemistry, Institute of Geology and Geophysics, Chinese Academy of Sciences.

3.2. Major and trace elements

The samples intended for major and trace element analysis were first crushed and ground to a particle size of less than 200 mesh. The oxides of major elements were measured via X-ray

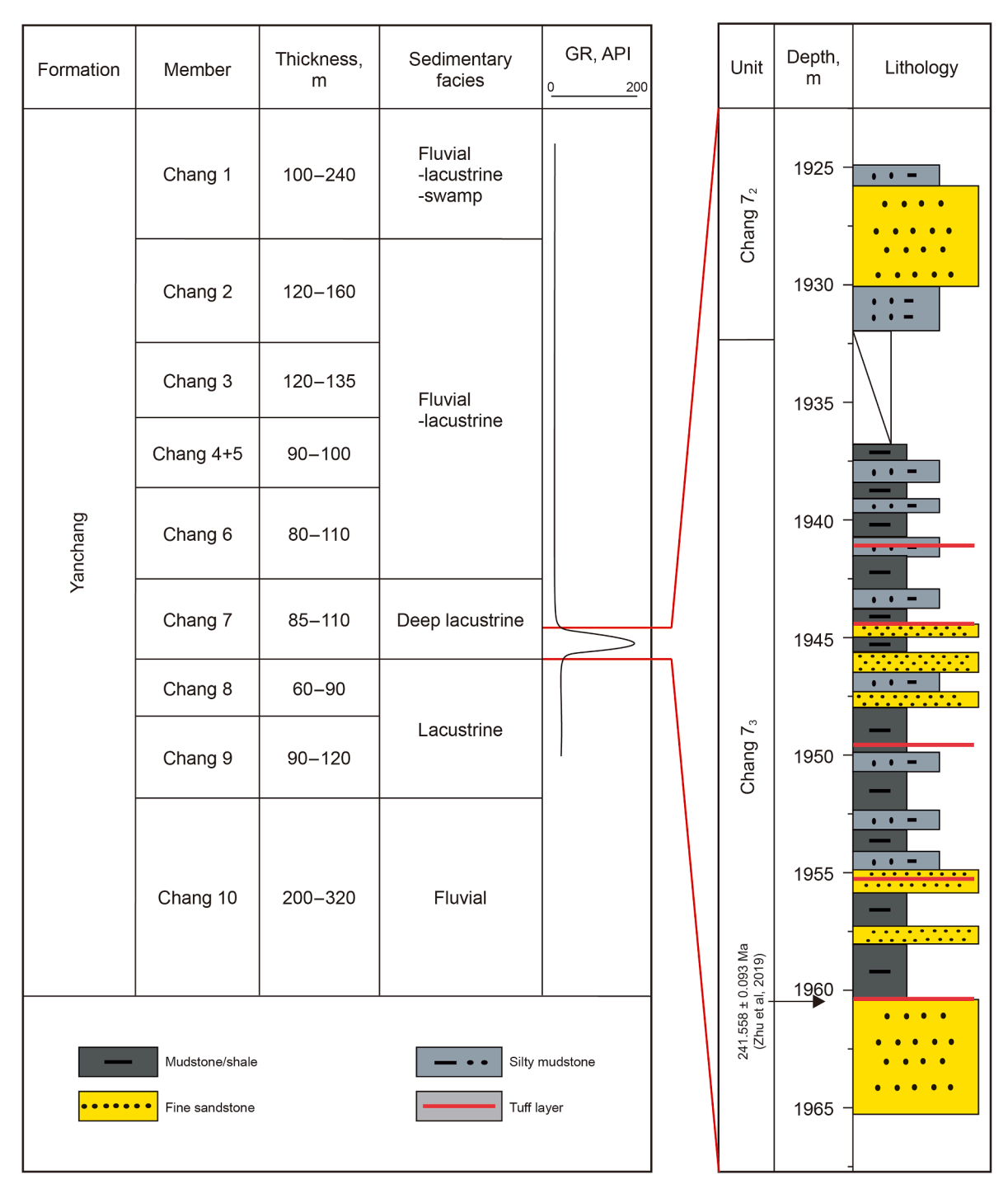


Fig. 2. Stratigraphic column for Ch7₃ of the Upper Triassic Yanchang Formation in Well B522 (Gao et al., 2023).

fluorescence (XRF) spectrometry, which revealed an analytical precision greater than 5%. Trace element concentrations were determined via a Finnigan MAT-252 inductively coupled plasma (ICP) mass spectrometry (MS) instrument. For trace element analysis, 50 mg of each sample was accurately weighed and reacted with 1 mL of HF and 0.5 mL of HNO₃ in screw-top polytetrafluoroethylene (PTFE)-lined stainless steel bombs at 185 °C for 24 h. The insoluble residues were then digested with 5 ml of 30% HNO₃ for 3 h at 130 °C and subsequently diluted to 25 mL, achieving an analytical precision exceeding 0.1% (Li et al., 2020).

3.3. Iron speciation

The weight percentage of pyrite sulfur extracted as a Ag_2S precipitate was used to stoichiometrically calculate Fepy via the Cr-reduction method (Canfield et al., 1986). Fe_{Carb}, Fe_{OX}, and Fe_{mag} were obtained through a sequential extraction procedure as described by Poulton and Canfield (Poulton and Canfield, 2005; Jin et al., 2016). These procedures were conducted at the State Key Laboratory of Biogeology and Environmental Geology, China University of Geosciences (Wuhan).

3.4. Organic Carbon Accumulation Rate (OCAR)

Li et al. (2023) introduced a bottom-up methodology for determining the OCAR. This approach utilized TOC and dry bulk density (DBD) measurements from 81 stations under the International Ocean Discovery Program (IODP), along with well-defined age models, to establish global organic carbon burial rates for the Neogene. (Li et al., 2023).

$$OCAR = SR \times TOC\% \times DBD \tag{1}$$

where *SR* is the sedimentation rate and where *DBD* is the dry bulk density.

The sedimentation rate (SR, cm/kyr) is a critical component of this calculation. A time series analysis of gamma-ray (GR) data from Ch73 was conducted to determine the SR. To reduce distortion in the low-frequency section of the spectra, long-term trends were removed from the original GR series via the rLOWESS method (smooth range: 20%-35%), as recommended by Cleveland (1979). A logarithmic transformation was applied to narrow the data range and minimize the influence of outliers in cases of excessive GR value ranges. The correlation coefficient (COCO) method was used to estimate the correlation between an astronomical solution and the power spectrum of the GR series in the depth domain, converting the raw GR data from depth measurements into a time-domain SR analysis. The SR with the highest correlation coefficient was deemed the most reliable. The evolutionary correlation coefficient method (eCOCO) was refined to track fluctuating SRs, integrating both COCO and sliding window techniques (Li et al., 2018; Wang et al., 2020; Wei et al., 2023). These analyses were performed via Acycle v 2.0 software (Li et al., 2019). For the analysis, an age of 241 Ma was selected for the bottom of Ch73, which was determined through zircon U-Pb dating via the ID-TIMS method (Zhu et al., 2019).

The DBDs of the core samples were measured via an electronic scale. The sample mass (m) was first measured in air and then in water, with a liquid density of 1 g/cm³, to calculate the density (ρ) of the sample via the appropriate equation. Measurements were conducted with an electronic scale (model ZZ-C30002) with a maximum capacity of 3000 g, a minimum display time of 20 d, and a precision of 0.01 g.

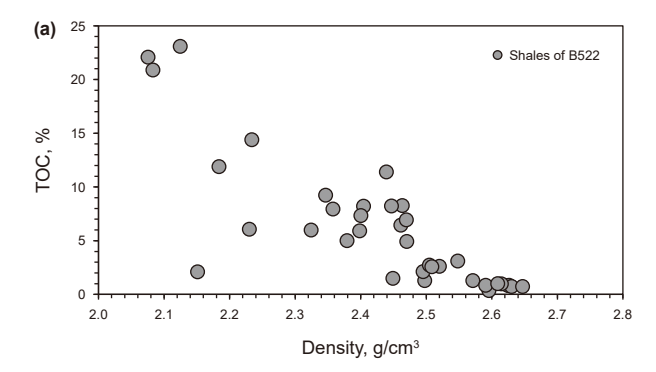
$$\rho = \rho_0 \frac{m}{m - m_1} \tag{2}$$

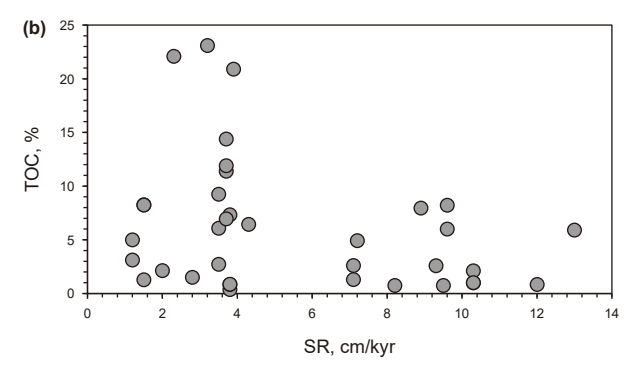
where ρ is the density of the sample, ρ_0 is the density of the water, m is the mass of the sample measured in air, and m_1 is the mass of the sample measured in water.

4. Results

4.1. Organic carbon burial

In the Ch7₃ samples, the TOC content varied from 0.37 to 23.10 wt% ($\bar{x}=6.12$ wt%) (Table 1). The density of the samples decreased as the OM content increased, which reflects the lower density of OM than that of the rock matrix. The sample densities ranged from 2.07 to 2.64 g/cm³ ($\bar{x}=2.43$ g/cm³) (Fig. 3(a)). The SRs in Ch7₃ ranged between 1.20 and 13.00 cm/kyr ($\bar{x}=5.51$ cm/kyr) (Fig. 3(b)). This finding aligns with previously reported average sedimentation rates of approximately 4–6 cm/kyr (Chen et al., 2020; Zhang et al., 2017). Notably, when the sedimentation rate exceeds 7 cm/kyr, there is a significant decrease in the OM content.





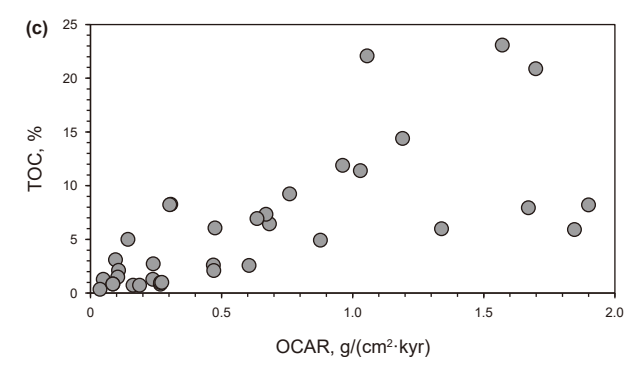


Fig. 3. Analyses of TOC, density, SR, and OCAR data for Ch7₃. (a) Crossplots of TOC versus density. (b) Crossplots of TOC versus SR. (c) Cross-plots of TOC versus OCAR.

The OCAR ranged from 0.04 to 1.90 g/(cm²·kyr) ($\bar{x} = 0.63$ g/(cm²·kyr)) (Fig. 3(c)).

4.2. Iron speciation

The total highly reactive iron (Fe_{HR}), defined as the sum of Fe_{py}, Fe_{carb}, Fe_{ox}, and Fe_{mag}, ranged from 0.44 to 12.08% ($\bar{x}=3.62\%$) (Table 1). Under reducing (anoxic) conditions, Fe_{HR} included additional contributions from Fe_{carb} and Fe_{py}, with Fe_{carb} values ranging from 0.22 to 3.45% ($\bar{x}=0.99\%$) and Fe_{py} values ranging from 0.03 to 10.16% ($\bar{x}=2.29\%$) (Fig. 4). The contents of Fe_{ox} and Fe_{mag} were relatively low, with Fe_{ox} ranging from 0.04 to 0.62 % ($\bar{x}=0.20\%$) and Fe_{mag} ranging from 0.01 to 0.40% ($\bar{x}=0.13\%$). All samples presented ratios of Fe_{HR} to total iron (Fe_T) (Fe_{HR}/Fe_T) exceeding 0.38. Some samples presented ratios of pyrite to Fe_{HR} (Fe_{Py}/Fe_{HR}) exceeding 0.8. These ratios suggest sediment accumulation over extended periods under an anoxic and iron-rich (nonsulphidic) water column, with occasional accumulation under sulphidic water columns.

Table 1The sample densities, SRs, OCAR and Bulk geochemical parameters of the Ch7₃ organic-rich shale in Well B522.

Sample	Depth, m	TOC, %	Density, g/cm ³	SR, cm/kyr	OCAR, g/(cm ² ·kyr)	P/Ti	Fe _{py} /Fe _{HR}	Mo _{EF}	U _{EF}
No.									
1	1964.2	1.30	2.57	7.10	0.24	0.14	0.02	1.14	0.41
2	1961.6	4.93	2.47	7.20	0.88	0.53	0.59	4.50	2.31
3	1960.9	8.23	2.40	9.60	1.90	0.51	0.83	5.15	1.50
4	1960.2	8.27	2.46	1.50	0.31	0.54	0.68	5.61	2.25
5	1959.8	8.24	2.45	1.50	0.30	0.29	0.80	5.83	2.92
6	1959.5	1.29	2.50	1.50	0.05	0.20	0.19	0.36	1.29
7	1958.3	22.10	2.08	2.30	1.05	4.13	0.88	44.17	20.83
8	1957.5	3.12	2.55	1.20	0.10	0.31	0.41	7.21	2.61
9	1956.8	5.01	2.38	1.20	0.14	0.46	0.74	13.19	6.18
10	1956.1	2.14	2.49	2.00	0.11	0.22	0.38	0.81	1.24
11	1955.7	1.51	2.45	2.80	0.10	0.21	0.16	0.74	1.94
12	1952.4	7.96	2.36	8.90	1.67	0.17	0.57	3.71	1.59
13	1951.5	23.10	2.12	3.20	1.57	1.61	0.78	155.94	59.52
14	1950.3	2.73	2.50	3.50	0.24	0.28	0.32	4.96	2.71
15	1950.0	6.08	2.23	3.50	0.47	0.32	0.80	27.02	5.17
16	1949.3	11.40	2.44	3.70	1.03	0.79	0.84	63.45	17.66
17	1947.3	6.45	2.46	4.30	0.68	0.46	0.86	28.50	8.17
18	1945.3	7.34	2.40	3.80	0.67	1.22	0.79	37.31	5.46
19	1944.8	11.90	2.18	3.70	0.96	1.34	0.79	38.67	13.15
20	1944.4	6.95	2.47	3.70	0.63	0.73	0.80	37.90	9.26
21	1943.2	20.90	2.08	3.90	1.70	1.37	0.79	103.64	30.28
22	1941.7	9.25	2.35	3.50	0.76	0.46	0.85	24.58	7.56
23	1941.0	0.37	2.60	3.80	0.04	0.20		2.78	2.49
24	1940.5	14.40	2.23	3.70	1.19	1.41	0.86	36.43	10.44
25	1939.8	0.85	2.63	3.80	0.08	0.21	0.04	1.00	1.02
26	1939.4	0.87	2.59	3.80	0.09	0.21	0.02	1.19	1.08
27	1938.4	0.85	2.62	12.00	0.27	0.21	0.03	1.09	1.04
28	1937.7	5.92	2.40	13.00	1.85	0.49	0.80	16.62	1.78
29	1931.4	2.62	2.52	7.10	0.47	0.30	0.08	6.12	1.58
30	1930.6	2.59	2.51	9.30	0.60	1.37	0.39	6.27	2.52
31	1929.8	0.75	2.63	8.20	0.16	0.28	0.03	2.00	0.99
32	1929.2	6.00	2.32	9.60	1.34	0.50	0.78	24.34	4.65
33	1928.4	0.99	2.61	10.30	0.27	0.23	0.14	2.79	1.06
34	1927.5	2.12	2.15	10.30	0.47	0.34	0.31	4.21	2.99
35	1927.0	1.01	2.61	10.30	0.27	0.23	0.05	1.30	1.09
36	1926.0	0.75	2.65	9.50	0.19	0.21	0.02	0.90	1.09

4.3. Major and trace element compositions

A total of 36 shale samples from Well B522 were analyzed for their major element compositions (Table 1). The samples presented variable concentrations of SiO₂ (31.51%–82.44%, $\bar{x} = 53.67$ %), Al₂O₃ $(7.75\%-22.38\%, \bar{x} = 14.71\%)$, CaO $(0.49\%-11.32\%, \bar{x} = 2.79\%)$, K₂O $(0.84\%-6.88\%, \bar{x} = 2.86\%)$, and Na₂O $(0.49\%-3.17\%, \bar{x} = 1.30\%)$. The loss on ignition (LOI) exhibited a wide range (5.18%-39.31%, $\bar{x} = 15.43\%$) and was negatively correlated with CaO (Fig. 5(a)) but positively correlated with total organic carbon (TOC) (Fig. 5(b)). This suggests that variations in the LOI are related primarily to the TOC content, Increases in both TOC and carbonate can lead to higher LOI values, resulting in lower concentrations of Al₂O₃, TiO₂, SiO₂, K₂O, and Na₂O. However, changes in carbonate or TOC contents do not affect the ratios of elements such as Al₂O₃/SiO₂ and Al₂O₃/TiO₂. The Al₂O₃/SiO₂ ratios of the mudrock samples varied within a narrow range (0.09–0.40, \bar{x} = 0.28) and were lower than those of the sandstone samples. The Al₂O₃/TiO₂ ratio also exhibited limited variation across most samples (22.15–175.28, \bar{x} = 42.68). In terms of trace element concentrations, the samples contained Y in the range of 3.63–45.80 ppm ($\bar{x} = 15.56$ ppm), Th from 2.99 to 28.39 ppm $(\overline{x} = 7.58 \text{ ppm})$, Sc from 0.73 to 10.55 ppm $(\overline{x} = 4.71 \text{ ppm})$, Zr from 56.18 to 201.55 ppm ($\bar{x} = 107.84$ ppm), and Nb from 7.69 to 17.42 ppm ($\bar{x} = 11.92$ ppm). Most samples presented Th/Sc, Th/Nb, Nb/Y, and La/Yb ratios ranging from 0.74 to 6.37 ($\bar{x} = 2.03$), 0.22 to 1.98 ($\bar{x} = 0.64$), 0.25 to 3.59 ($\bar{x} = 1.14$), and 3.36 to 31.14 ($\bar{x} = 11.04$), respectively.

5. Discussion

5.1. Dynamic carbon sequestration during Ch7₃

During hothouse periods, primary carbon repositories are found in continental margins and specific deep ocean regions. For example, marine environments accounted for approximately 82% of organic carbon sequestration during Oceanic Anoxic Event 2 (Owens et al., 2018). Other potential carbon sinks include contemporary lakes (such as the Oyubari area in Japan) (Hasegawa, 1997), terrestrial soils and coalbeds (e.g., Alton coal in Utah, US) (Laurin et al., 2019), and marine areas with moderate to low TOC values (<1 wt%).

The Ordos Basin presented an average OCAR (OCAR) of 0.68 g/(cm²-kyr) during the deposition of Ch73, as calculated via Eq. (1) (Fig. 6). Although the initial sedimentation of Ch7 occurred in semideep to deep lake facies covering an area of approximately 65,000 km², it sequestered an estimated 0.27 trillion tons (Tt) of organic carbon, as determined via Eq. (3).

$$OC MAS (Tt) = \overline{OCAR} \times S \times T \times 10^{-5}$$
(3)

where $S(\mathrm{km}^2)$ represents the sedimentary area of the Ordos Basin, and T (million years, Myr) denotes the sedimentation time for Ch7₃. According to previous analyses, Ch7₃ in well B522 was deposited at a thickness of 33 m (1932–1965 m), with an average SR of 5.51 cm/kyr. Consequently, the sedimentation time for Ch7₃ in well B522 is estimated to be approximately 0.6 Myr.

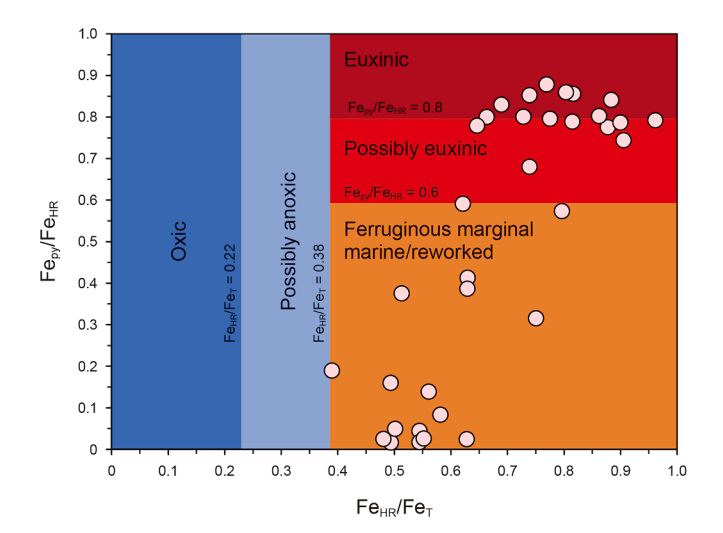


Fig. 4. Diagnostic fields of Fe_{py}/Fe_{HR} and Fe_{HR}/Fe_{T} . The red circle represents the samples of $Ch7_3$ (Image version modified from reference (Poulton, 2021)).

5.2. Environmental and biological drivers of OM enrichment in $Ch7_3$

5.2.1. Paleo-weathering conditions

The chemical index of alteration (CIA) is commonly used to assess the degree of chemical weathering (Mclennan, 1993). The CIA is calculated via the following formula:

$$CIA = \left(\frac{Al_2O_3}{Al_2O_3 + Na_2O + CaO^* + K_2O}\right) \times 100 \tag{4}$$

where CaO* represents the amount of CaO present in silicates (Nesbitt and Young, 1982). According to McLennan and Taylor (1991), if the adjusted CaO value [CaO(adjusted) = mol CaO $-(10/3 \text{ mol } P_2O_5)$] is greater than Na₂O. Otherwise, the CaO* value is equivalent to the CaO(adjusted) value (Mclennan, 1993).

In this study, the CIA values of the samples decreased due to the effects of K-metasomatism. Fedo et al. (1995) demonstrated that "premetasomatic" compositions can be identified on A-CN-K diagrams by projecting each data point back to its original position (Fedo et al., 1995). Following this interpretation, we applied the calculations proposed by Panahi (Panahi et al., 2000) to determine the corrected K₂O value K₂O*. K₂O* can be calculated as follows:

$$K_2O^* = \frac{m \times Al_2O_3 + m \times (Na_2O + CaO^*)}{1 - m}$$
 (5)

where $m = \frac{K_2O}{Al_2O_3 + Na_2O + CaO^* + K_2O}$ for the parent sample. The obtained K_2O^* was then used to calculate the K-metasomatism-corrected CIA* value.

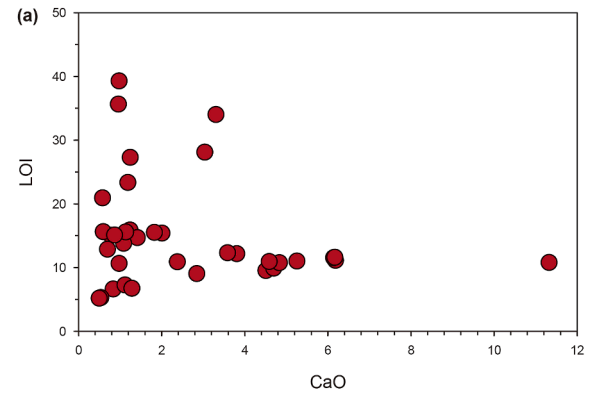
Some samples deviate from the ideal weathering trend line on the A-CN-K diagram. (Fig. 7), indicating that K-metasomatism influenced the sediment (Fedo et al., 1995; Lu et al., 2020). This phenomenon likely contributed to the reduced CIA values (Yang et al., 2022) (Fig. 8(a)). Consequently, K-metasomatism was corrected via the method proposed by previous researchers, resulting in the CIA* (corrected CIA) (Fedo et al., 1995). Fedo demonstrated that the preparental composition could be identified by projecting data points back to their original positions on the A-CN-K diagram. (Fedo et al., 1995).

High CIA* values typically indicate intense chemical weathering conditions, which generally occur in warm and humid climates characterized by significant rainfall and continental runoff (Montero-Serrano et al., 2015). Sediments with CIA values of 100–80, 80–70, and 70–50 reflect strong, intermediate, and weak weathering conditions in the source area, respectively (Nesbitt and Young, 1982). The CIA* values for Ch7₃ ranged from 73.6 to 83.8 ($\bar{x} = 78.2$), suggesting that these sediments formed under intermediate weathering conditions (Fig. 8(d)).

The interplay among global tectonics, climatic patterns, and significant geological events is crucial in controlling OM enrichment in the Ordos Basin. During the Triassic period, the northward drift of the supercontinent Pangaea exposed more land to a warm and humid climate (Landwehrs et al., 2022). In the Middle Triassic, intensified chemical weathering processes within the Tethys resulted in increased ratios of Al/Ti, K/Ti, Rb/Sr, Rb/K, and Fe/Mn in the organic-rich shale of the Ch7 section of the Ordos Basin (Trotter et al., 2015; Chu et al., 2020; Liu, 2021). The occurrence of humid climatic events during the late Ladinian to Carnian periods may have accelerated the release of latent heat from the Tethys Ocean, thereby increasing monsoonal precipitation and continental weathering in the Tethys domain (Scotese et al., 2021; Liu et al., 2024). This increased chemical weathering supplied additional nutrients to the lake, significantly increasing primary productivity in Ch7₃.

5.2.2. Primary productivity

Several trace elements, particularly phosphorus (P), serve as useful proxies for reconstructing primary productivity (Tribovillard et al., 2006; Schoepfer et al., 2015). P is a vital nutrient for algal growth (Vink et al., 1997; Slomp et al., 2004). By eliminating the influence of terrigenous clastic materials, the P/Ti ratio is widely utilized as an indicator of paleoproductivity (Tribovillard



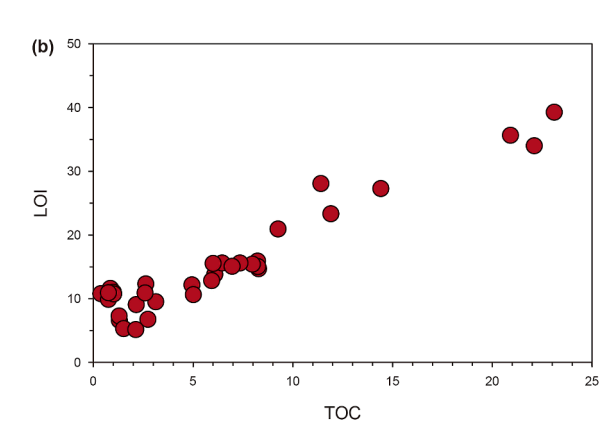


Fig. 5. Analyses of LOI, CaO and TOC data for Ch73. (a) Cross-plots of the LOI versus CaO. (b) Cross-plots of LOI versus TOC.

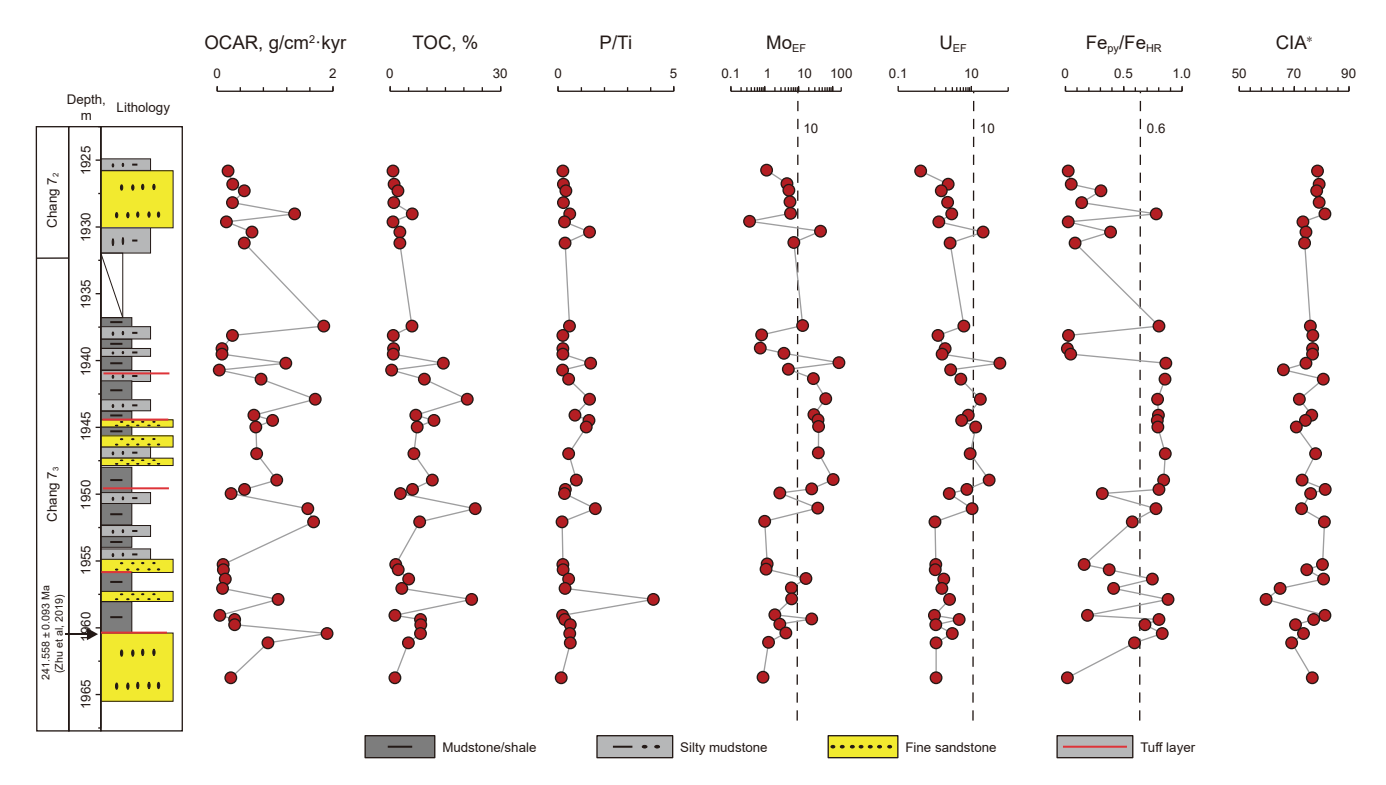


Fig. 6. Vertical variations in the OCAR, TOC, P/Ti, Mo_{EF}, U_{EF}, Fe_{DV}/Fe_{HR}, and CIA* in Ch7₃ of Well B522.

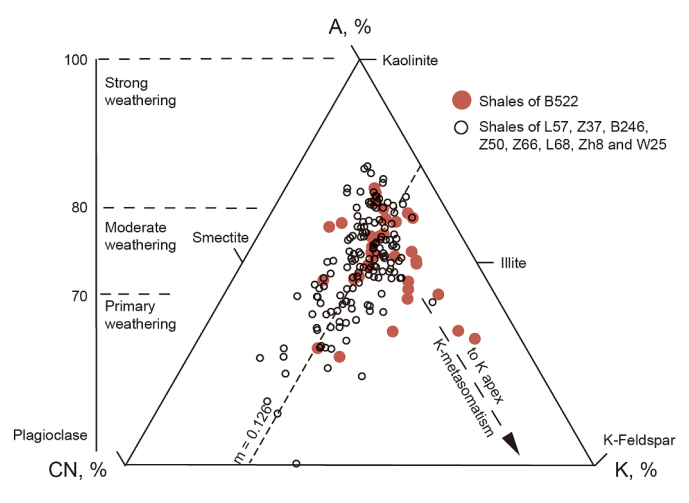


Fig. 7. A-CN-K (Al₂O₃-CaO*+Na₂O-K₂O) diagram with the CIA scale of Ch7₃. The red circles represent the results of this study, while the black hollow circles represent the data collected from the literature. Gray data points from references (Yuan et al., 2021, 2022; Liu et al., 2024). Image version modified from reference (Zhang et al., 2017)).

et al., 2006). Elevated P/Ti ratios are indicative of high paleoproductivity.

The P/Ti ratios of the lower Ch7₃ oil shale range from 0.14 to 4.13 ($\bar{x}=0.62$), which are significantly higher than the average P/Ti ratio of the Post-Archean Australian shale (PAAS) (0.13) (McLennan and Taylor, 1991), indicating high productivity (Fig. 8(b) and (e)). This finding suggests that the lake in which the Upper Triassic Ch7₃ organic-rich deposits accumulated was characterized by high primary productivity. In aquatic environments with high primary productivity, a substantial amount of OM accumulates on the lakebed following the death of numerous organisms. The

mineralization of some of this OM leads to reduced oxygen levels at the lake bottom, creating anoxic conditions that favor the preservation of OM, which may further evolve into euxinic conditions.

5.2.3. Redox conditions

The concentrations of certain elements, such as molybdenum (Mo), uranium (U), and iron (Fe), in sedimentary rocks serve as indicators of the redox conditions that prevailed during sediment deposition (Tribovillard et al., 2006). Consequently, the enrichment and ratios of these elements can be used to reconstruct the paleoenvironment (Algeo and Ingall, 2007; Montero-Serrano et al., 2015).

Mo and U concentrations in sediments are particularly valuable as redox proxies, as their uptake rates increase under more reducing conditions (Tribovillard et al., 2006; Algeo and Tribovillard, 2009). The enrichment factor (EF) is used to estimate the degree of elemental enrichment in shale and is calculated as follows:

$$X_{EF} = \frac{(X/AI)_{sample}}{(X/AI)_{PAAS}}$$
 (6)

where X and Al represent the weight percent concentrations of X and Al, respectively (Tribovillard et al., 2006, 2012; Algeo and Tribovillard, 2009; Little et al., 2015). The samples were normalized to the post-Archean average shale (PAAS) compositions (McLennan and Taylor, 1991). EFs > 1.0 indicate elemental enrichment relative to the PAAS concentration. Specifically, EFs > 3 represent detectable enrichment, whereas EFs > 10 indicate moderate to strong enrichment (Algeo and Tribovillard, 2009).

Previous discussions regarding the sulfidation boundaries of Fe_{py}/Fe_{HR} in marine basins have focused primarily on samples from marine black shales, which limits the applicability of these

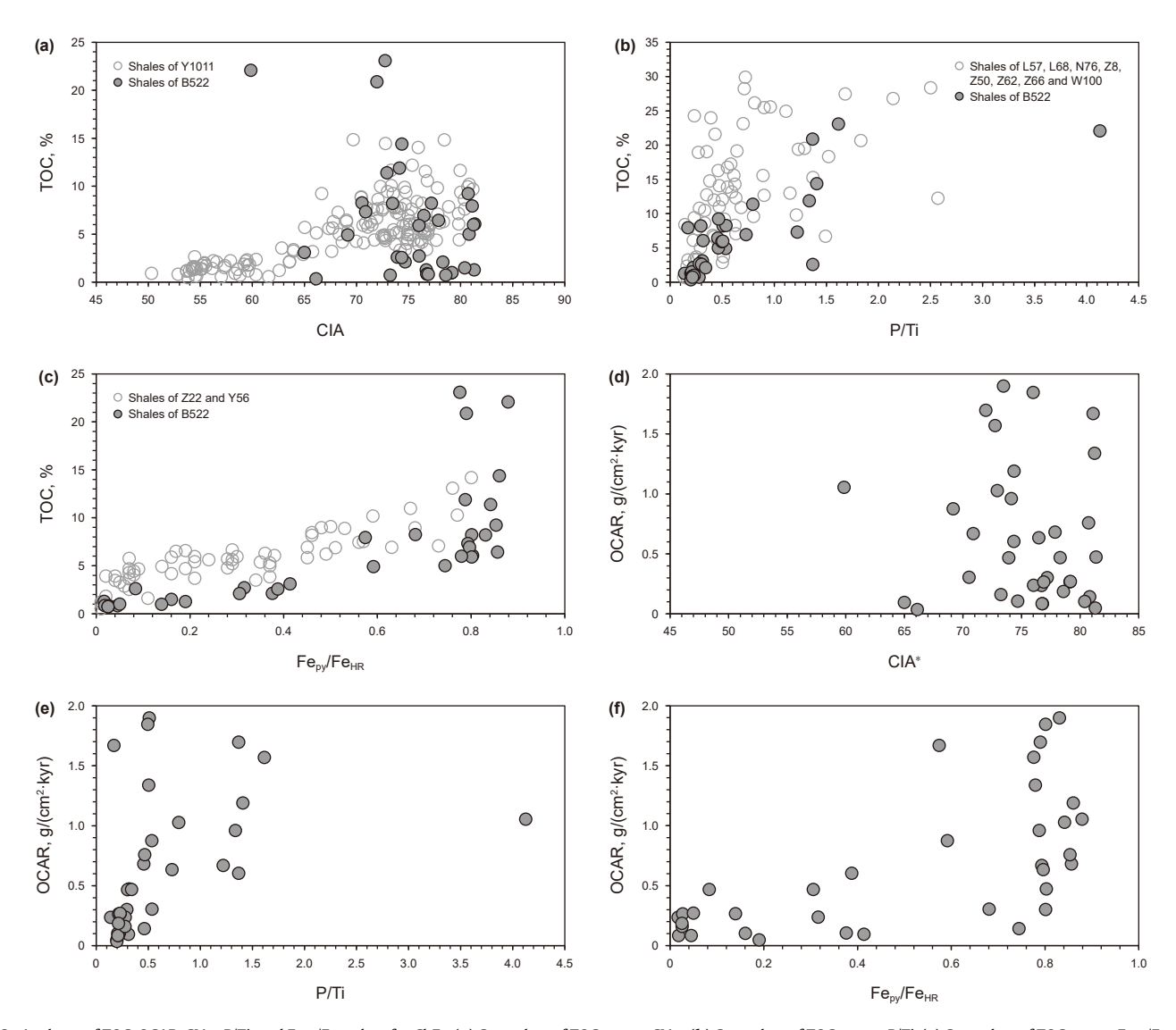


Fig. 8. Analyses of TOC, OCAR, CIA*, P/Ti, and Fe_{py}/Fe_{HR} data for Ch7₃. (a) Crossplots of TOC versus CIA*. (b) Crossplots of TOC versus P/Ti. (c) Crossplots of TOC versus Fe_{py}/Fe_{HR}. (d) Cross-plots of OCAR versus CIA*. (e) Cross-plots of OCAR versus Fe_{py}/Fe_{HR}. (Gray data points from references (Yuan et al., 2021, 2022; Liu et al., 2024)).

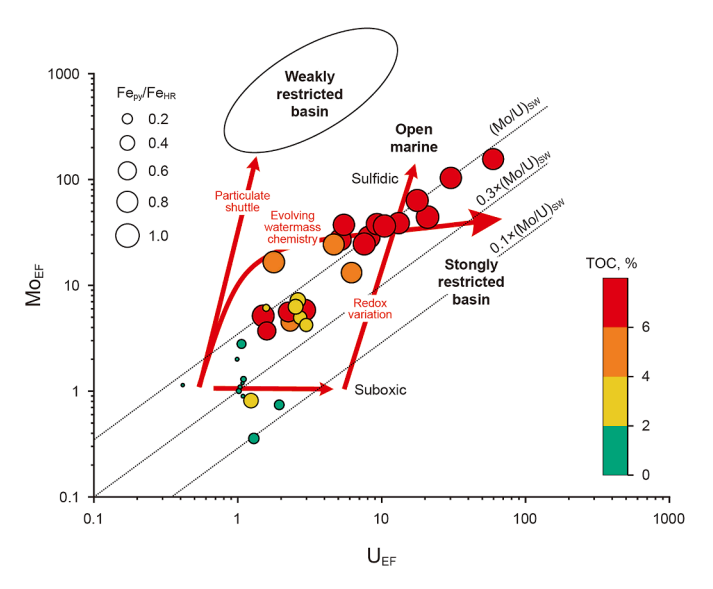
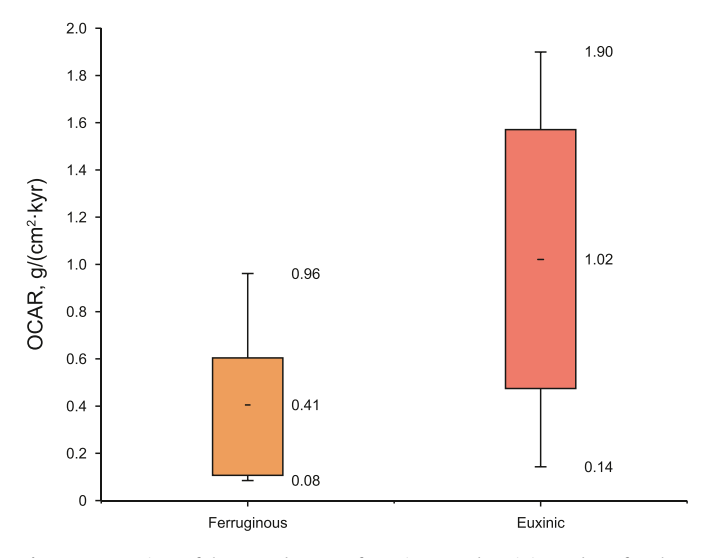


Fig. 9. Analyses of Mo_{EF} , U_{EF} , TOC, and Fe_{py}/Fe_{HR} data for $Ch7_3$ (Image version modified from reference (Algeo and Ingall, 2007).

boundaries to lacustrine basins (Poulton and Canfield, 2011; Raiswell and Canfield, 2012; Raiswell et al., 2018). Compared with marine basins, lacustrine basins are smaller, exhibit greater structural diversity, and have more pronounced segmentation, resulting in distinct environmental characteristics. In marine basins, pyrite formation primarily arises from two sources: the occurrence of sulfate reduction reactions in iron-rich upper layers, where OM is degraded, producing locally supersaturated H₂S zones that lead to pyrite precipitation (Canfield et al., 1996). The vertical movement of water transports dissolved iron to lower sulfide-containing layers or sulfides to iron-rich areas. For example, eddy diffusion in the Black Sea facilitates the downward transport of iron to the sulfide zone and the upward movement of sulfides to iron-rich areas, thereby promoting pyrite precipitation (Brewer and Spencer, 1974; Lewis and Landing, 1991). Compared with lacustrine basins, the larger scale of vertical circulation in marine basins contributes to a greater abundance of sulfide phases. Therefore, the sulfidation boundary of Fe_{pv}/Fe_{HR} in lacustrine basins should be considered lower than that in marine basins



 $\textbf{Fig. 10.} \ \ \text{Comparison of the OCAR between ferruginous and euxinic products for Ch7_3.}$

(Fig. 8(c) and (f)). In this study, $Fe_{py}/Fe_{HR} > 0.6$ is proposed as an empirical index for identifying potential euxinic conditions based on the Fe_{py} and Fe_{HR} contents in the shale layers (Poulton, 2021).

Based on the criteria established for identifying sulfidic environments, the sedimentary environments of the samples were classified into weakly oxidizing conditions (Fe_{HR}/Fe_T < 0.38, $Mo_{EF} < 1$, and $U_{EF} < 1$), ferruginous conditions (Fe $_{py}$ /Fe $_{HR} < 0.6$, $Fe_{HR}/Fe_T > 0.38$, $Mo_{EF} > 1$, and $U_{EF} > 1$), and eunixic conditions $(Fe_{DV}/Fe_{HR} > 0.6, Fe_{HR}/Fe_{T} > 0.38, Mo_{EF} > 10, and U_{EF} > 10)$ (Fig. 9). The OCAR under euxinic conditions ranged from 0.14 to 1.90 g/ $(cm^2 \cdot kyr)$ ($\bar{x} = 1.02 \text{ g/(cm}^2 \cdot kyr)$), whereas under ferruginous conditions, it ranged from 0.08 to 0.96 g/(cm²·kyr) ($\bar{x} = 0.40$ g/ (cm²·kyr)) (Fig. 10). Although the average OCAR under euxinic conditions is approximately twice that under ferruginous conditions, euxinic conditions may have existed only in the sedimentary center during the deposition of Ch73 (Wang et al., 2024). Consequently, the extensive area of ferruginous conditions throughout the lake basin results in a significantly greater amount of organic carbon burial under ferruginous conditions than under euxinic conditions.

5.3. Impact of volcanism on the OCAR of Ch7₃

Intense volcanism is frequently linked to black shales in the Ordos Basin, indicating that tuff layers may affect the organic carbon content of these shales (Yuan et al., 2019; Gou and Xu, 2023; Liu et al., 2024; Wang et al., 2024). Previous research has demonstrated that volcanic eruptions and tephra can enhance the preservation of OM in ancient black shales (Liu et al., 2022b; Jin et al., 2023) (Fig. 11).

There are no universally applicable indicators for identifying volcanism; rather, a combination of multiple indicators is necessary to confirm its presence (Kiipli et al., 2013). Compared with the surrounding shale, bentonite has significantly different material sources and mineral compositions. Volcanic ash typically contains relatively high concentrations of elements such as Zr, Hf, Al, K, and Mg, whereas Si, Ni, and V are present in relatively low abundances. The presence of volcanism can be assessed via the following criteria: Zr > 160 ppm, Hf > 2.8 ppm, Zr/Cr > 1.0, $K_2O/Rb > 0.02$, Zr/Cr > 1.0 $Al_2O_3 > 6.0$, $Cr/Al_2O_3 < 10$, $V/Al_2O_3 < 20$, $Ni/Al_2O_3 < 10$, and $SiO_2/$ $Al_2O_3 < 5.0$ (Yang et al., 2022) (Fig. 12). These nine indicators are categorized into two groups. One category exhibits a positive correlation with the input of volcanic materials, while the other demonstrates a negative correlation. By applying dimensionality reduction to the indicators, a single representative indicator can be derived to quantify volcanic intensity (Fig. 13). Following principal

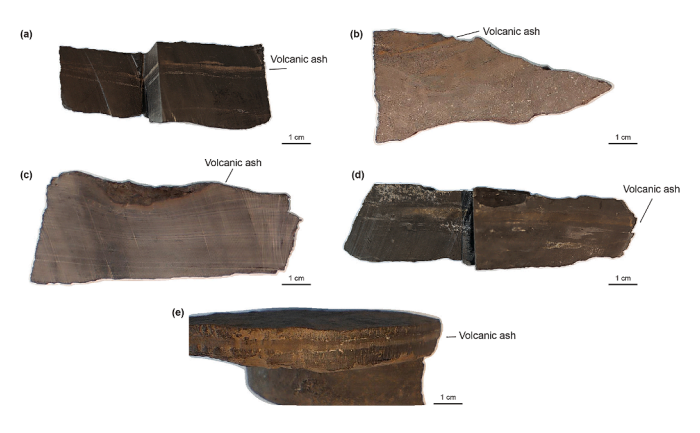


Fig. 11. Samples with tuffaceous banding for $Ch7_3$ of Well B522: (a)–(f) The visual record of volcanic activity in $Ch7_3$ is evident in the development of tuff layers within the shale, with some layers reaching millimeter-scale thickness.

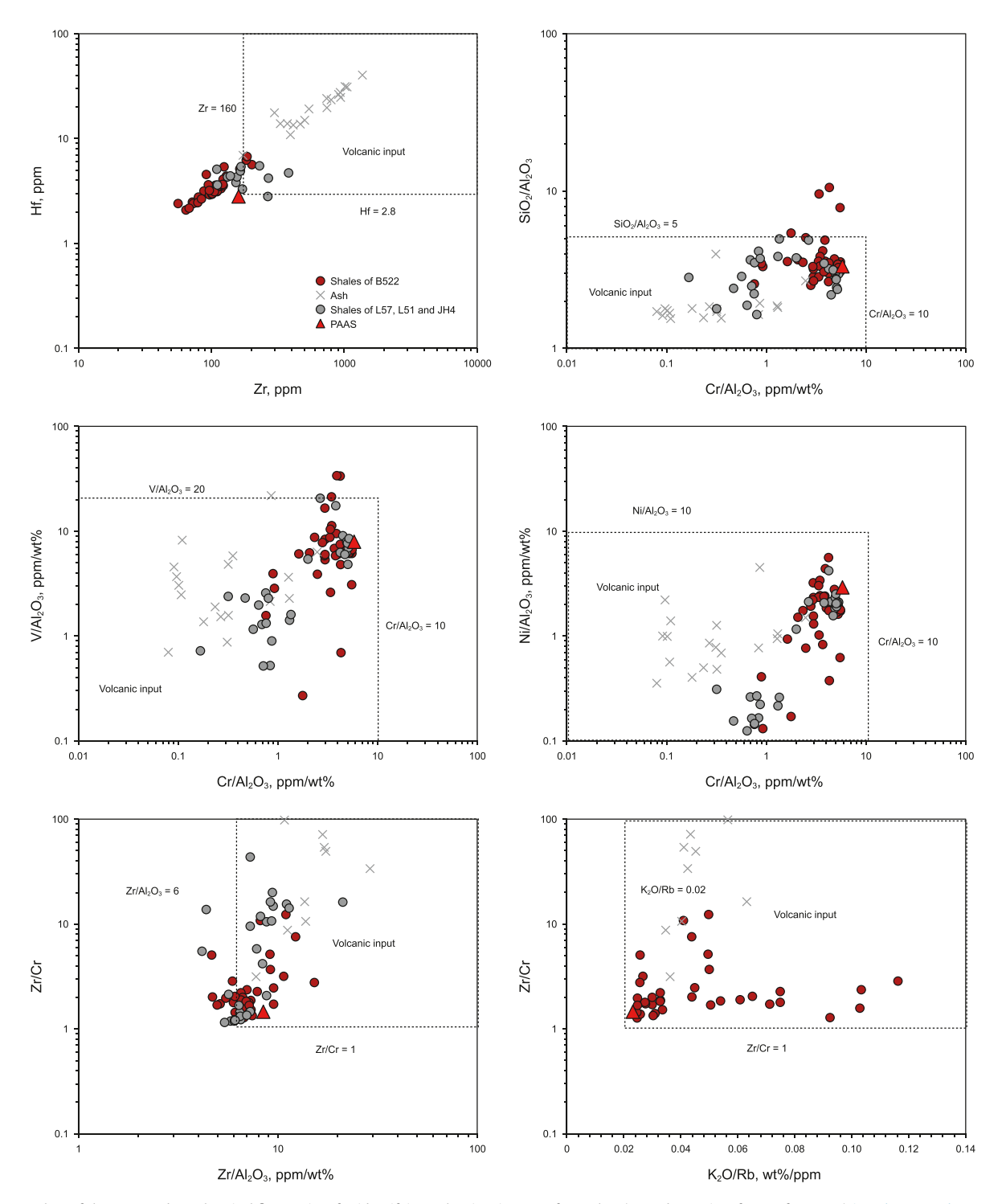


Fig. 12. Cross plots of the proposed geochemical fingerprints for identifying volcanism in strata from Ch7₃ (Gray data points from references (Li et al., 2020; Zhang et al., 2009). The volcanic ash data comes from reference (Yang et al., 2019). Image version modified from reference (Yang et al., 2022)).

component analysis (PCA) on data collected from 36 shale samples and volcanic ash samples obtained during the survey, the volcanic intensity index (F) derived from dimensionality reduction (Fig. 14), is calculated as follows:

$$F = 0.74 \times F_1 {+} 0.26 \times F_2$$

 $\begin{array}{l} F_2 = 0.08 \times Zr/Cr + 0.07 \times Zr/Al_2O_3 + 0.48 \times Ni/Al_2O_3 + 0.48 \times V/\\ Al_2O_3 + 0.04 \times K_2O/Rb - 0.02 \times Cr/Al_2O_3 - 0.30 \times SiO_2/\\ Al_2O_3 + 0.08 \times Hf + 0.10 \times Zr \end{array}$

where F_1 and F_2 represent the principal component 1 and principal component 2. The volcanic ash data comes from reference (Yang et al., 2019).

A comprehensive analysis of geochemical signatures reveals that Ch7₃ has been influenced by varying degrees of volcanic material input. Most sample data points plot within the volcanic material input zone. However, the Zr contents of the majority of

samples are less than 160 ppm, which is likely due to lower sedimentation rates and the presence of volcanic arc magmatic rocks as the source. During the MiddleLate Triassic Qinling orogeny, extensive magmatic activity occurred, which was divided into two distinct phases (approximately 235–250 Ma and 185–235 Ma) (Cohen et al., 2013). Ch7₃ was deposited during the early stage of this magmatic activity. The early granitic rocks predominantly exhibit I-type characteristics, primarily consisting of quartz diorite and tonalite, some of which have elevated Sr/Y ratios, indicative of products resulting from the northward subduction of the Mianlue Ocean (Dong et al., 2012; Wang et al., 2013).

Zr, Zr/Al₂O₃, and Zr/Cr exhibit similar variation patterns. Specifically, from the bottom to the top of Ch7₃, the occurrence of Zr, Zr/Cr, and Zr/Al₂O₃ gradually decreases (Fig. 13). The high peak at the bottom of Ch7₃ indicates intensive volcanic material input. During Ch7₂, these indicators gradually decreased to levels typical of normal shales, suggesting weak volcanism. These findings indicate that the Ordos region experienced strong volcanism during Ch7₃, followed by much weaker volcanic activity.

Based on a comprehensive analysis of the geochemical fingerprints, the volcanic eruptions in Ch7₃ and Ch7₂ of Well B522 were characterized by three distinct stages. Intensive volcanism

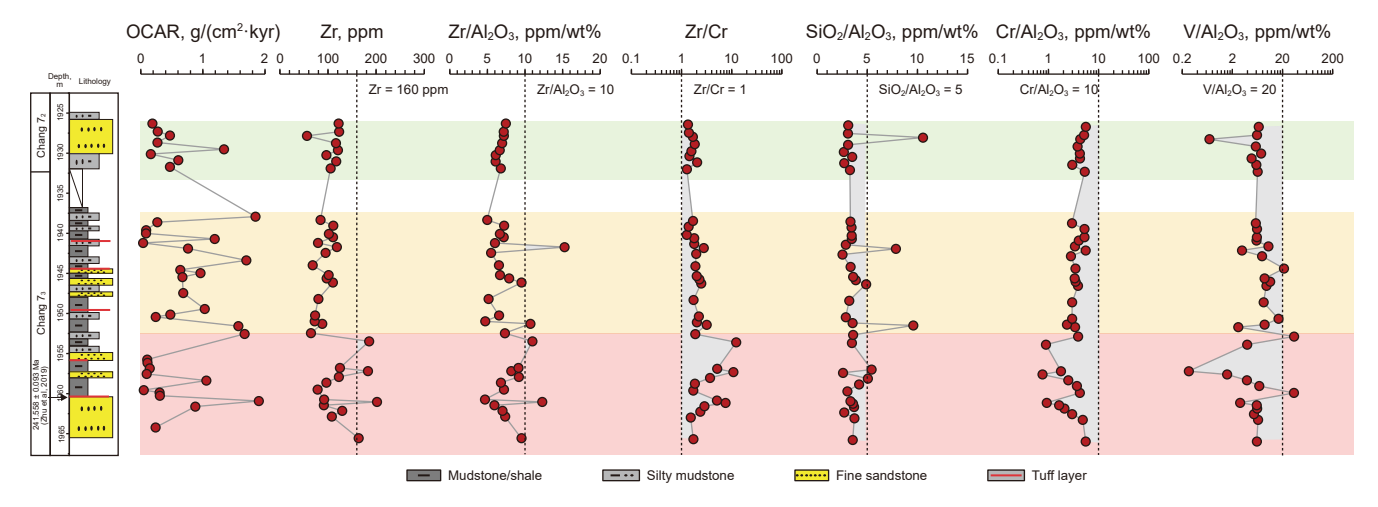


Fig. 13. Stratigraphic distributions of the proposed geochemical fingerprints of the volcanism in well B522.

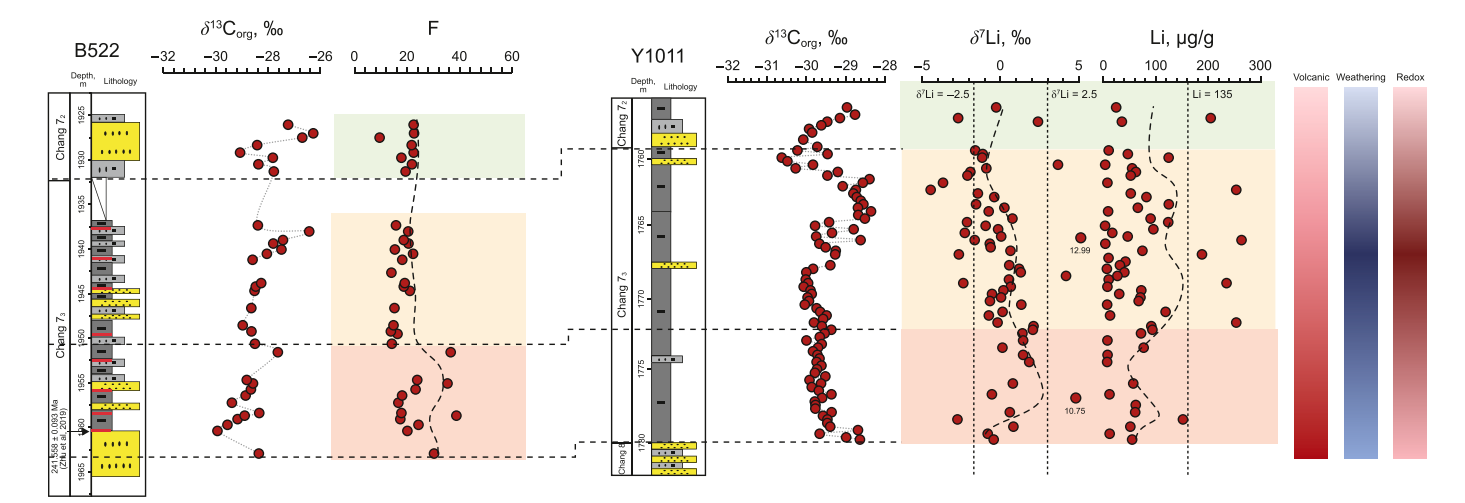


Fig. 14. Stratigraphic distributions of the proposed geochemical fingerprints of the volcanism in well B522 and well Y1011 (The carbon isotopes of B522 are from the reference (Wang et al., 2024); The carbon isotopes, δ^7 Li values and Li contents of Y1011 are from the reference (Liu et al., 2024)).

occurred at the base of Ch7₃ (1964.2–1952.4 m, indicated by red shading in Fig. 13), followed by a period of weaker eruptions during the upper section of Ch7₃ (1952.4-1937.7 m, indicated by orange shading in Fig. 13). The lowest Zr/Al₂O₃ and Zr/Cr ratios indicate the weakest volcanic activity at the base of Ch72 (1937.7-1926.0 m, indicated by the green shading in Fig. 13). During periods of intense volcanic activity, the average OCAR at the bottom reaches 0.57 g/(cm²·kyr) (red shading, ranging from 0.05 to 1.90 g/(cm²·kyr)). In contrast, during subsequent periods of weaker volcanic activity, the average OCAR peaks at 0.76 g/ (cm²·kyr) (yellow shading, ranging from 0.04 to 1.84 g/(cm²·kyr)). When volcanic activity is at its lowest level, the average OCAR also diminishes, reaching a minimum of 0.47 g/(cm²·kyr) (green shading, ranging from 0.16 to 1.34 g/(cm²·kyr)). The boundary of stages could be separated through the carbon isotope excursion (CIE) event (Fig. 14).

The differences in OCAR across various modes of volcanic activity may be attributed to both short-term and delayed effects on shale. The rapid deposition of volcanic ash during intense volcanic activity at the bottom of Ch7₃ led to the dilution of OM, which results in high δ^7 Li values (Fig. 14). During this period, the water

column experiences brief turbulence (Lu et al., 2021), which results in a lower OCAR during periods of airborne volcanic ash deposition (Lin et al., 2022). Concurrently, volcanic activity directly introduces nutrients and screens primary producers, creating a stress-free environment conducive to the emergence of screened algae (Yin et al., 2024). Although the high productivity triggered in a short time frame is offset by the negative impacts of volcanic activity, this results in a net increase in the OCAR (Fig. 15(c)). The moderate volcanic activity at the top of Ch73 can be considered influenced by volcanoes of appropriate intensity. The negative impact of volcanic activity is relatively low. The accumulated impact of volcanic activity on the intensity of chemical weathering has facilitated the input of nutrients from continental weathering into the lake basin, thereby promoting increased productivity (Liu et al., 2024), which results in high Li contents (Fig. 14). This extremely high productivity transformed the water column into euxinic conditions or led to the formation of the metalimnetic oxygen minimum (MOM) areas (Bian et al., 2025). Even though BSR consumes a greater amount of OM under euxinic conditions (Liu et al., 2021), extensive euxinic conditions provide favorable preservation conditions for OM deposition, resulting in a

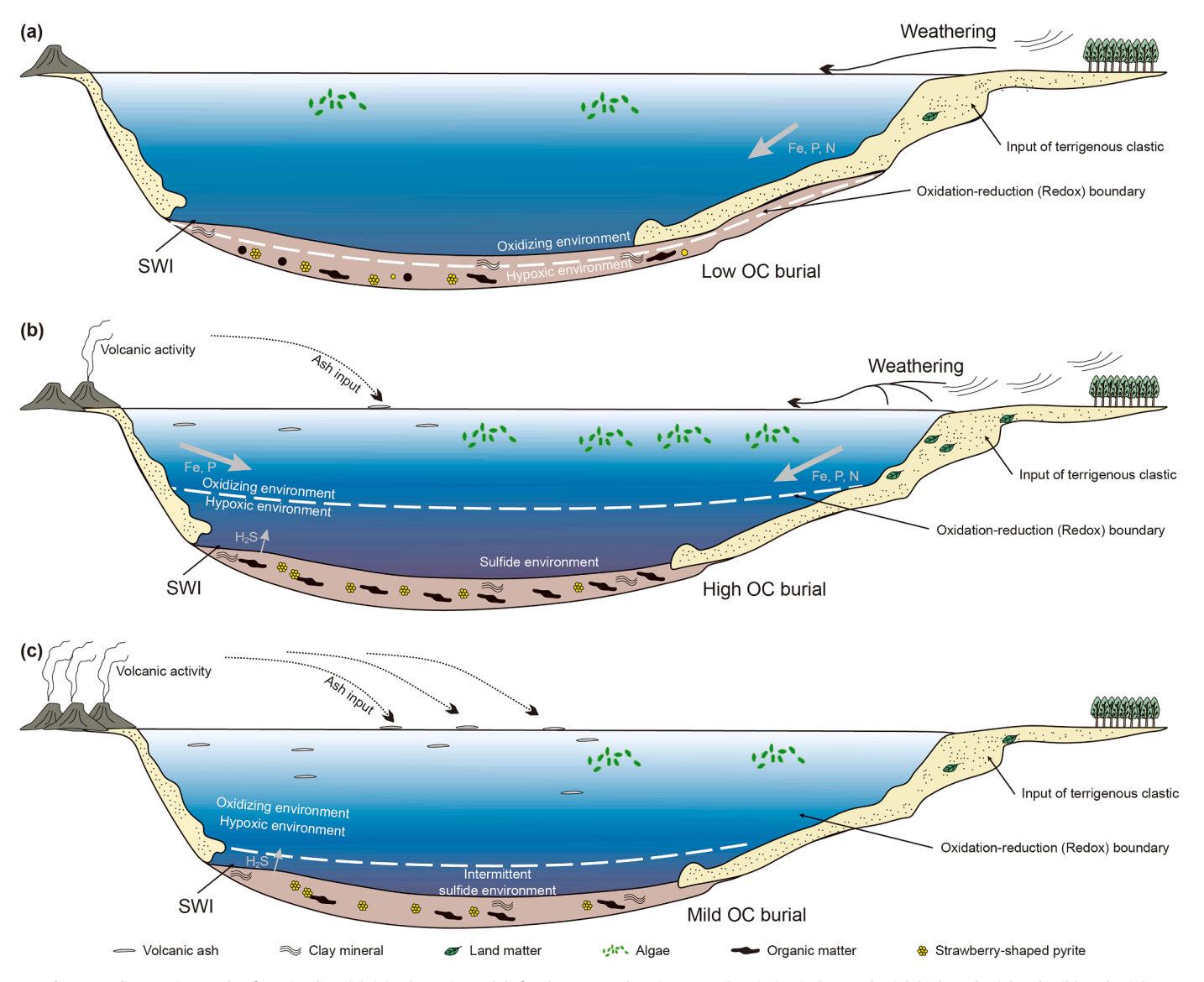


Fig. 15. Sedimentation mode of OM in Ch7₃. (a)–(c) schematic models for the proposed environmental variation in low OC burial, high OC burial and mild OC burial.

significant increase in the OCAR (Fig. 15(b)) (Lu et al., 2019). At the bottom of Ch7₂, volcanic activity is the weakest. The continuous decline in volcanic activity results in reduced weathering intensity, which limits nutrient input. As productivity gradually decreases, the extent of euxinic conditions also decreases, thereby constraining OM deposition to some degree (Fig. 15(a)). Under the influence of volcanic activity, Ch7₃ has developed a unique sedimentary pattern in which intense volcanic activity has led to a limited increase in the OCAR due to rapid sedimentation and dilution of OM. However, the combination of appropriate volcanic activity and nutrient input from continental weathering has resulted in a significant increase in the OCAR.

6. Conclusion

- 1) The SRs obtained from the time series analysis of the GR data and the measured sample density indicate a dynamic OCAR ranging from 0.04 to 1.90 g/(cm²·kyr) for Ch7₃. Based on the average OCAR (0.68 g/(cm²·kyr)) of Ch7₃, the total amount of organic carbon burial is estimated to be 0.27 Tt, considering the semideep to deep lake facies area (65,000 km²) and sedimentation duration (\approx 0.6 Myr).
- 2) Volcanic activity and high productivity can lead to the formation of eunixic conditions, thereby increasing the OCAR. According to the classification of iron speciation into ferruginous conditions and eunixic conditions, the OCAR was 2.49 times greater under eunixic conditions (ranging from 0.14 to 1.90 g/ (cm²-kyr), $\bar{x} = 1.02$ g/(cm²-kyr)) than under ferruginous conditions (ranging from 0.08 to 0.96 g/(cm²-kyr), $\bar{x} = 0.41$ g/ (cm²-kyr)).
- 3) The volcanic intensity index and corresponding OCAR suggest that when the intensity of volcanic activity is moderate, it is more conducive to the burial of OM in the lake basin. The more developed the layers of tuff are, the stronger the dilution of OM by rapidly deposited volcanic ash, and the water column during this period experiences brief turbulence, which is not conducive to the enrichment of OM. However, the direct input of nutrients from volcanic activity and the input of continental nutrients that promote weathering are beneficial for improving productivity. Based on the short-term and delayed effects of volcanic activity on shale, priority should be given to developing layers with moderately developed tuff laminations in the process of oil and gas development.

CRediT authorship contribution statement

Jia-Hong Gao: Writing – original draft, Methodology, Conceptualization. **Zhi-Jun Jin:** Writing – review & editing, Methodology, Conceptualization. **Xin-Ping Liang:** Writing – review & editing, Methodology, Conceptualization.

Declaration of competing interest

The authors declare that they have no known competing financial interests or personal relationships that could have appeared to influence the work reported in this paper.

Acknowledgement

This work is supported by the National Natural Science Foundation of China (Grant No. 42090025), and the National Key R&D Program of China (2023YFF0806200).

References

- Algeo, T.J., Ingall, E., 2007. Sedimentary C_{org}:P ratios, paleocean ventilation, and Phanerozoic atmospheric pO₂. Paleogeogr. Paleoclimatol. Paleoecol. 256, 130–155. https://doi.org/10.1016/J.PALAEO.2007.02.029.
- Algeo, T.J., Shen, J., 2023. Theory and classification of mass extinction causation. Natl. Sci. Rev. 11 (1), nwad237. https://doi.org/10.1093/nsr/nwad237.
- Algeo, T.J., Tribovillard, N., 2009. Environmental analysis of paleoceanographic systems based on molybdenum-uranium covariation. Chem. Geol. 268, 211–225. https://doi.org/10.1016/j.chemgeo.2009.09.001.
- Bian, L., Wang, X., Chappaz, A., Xiong, Z., Ye, M., Zhang, S., Zhao, W., 2025. Elemental-organic geochemical evidence for the lacustrine metalimnetic oxygen minimum dynamics in the Mid-Late Triassic Chang 7 shales. Earth Planet Sci. Lett. 651, 119153. https://doi.org/10.1016/j.epsl.2024.119153.
- Bos, R., Zheng, W., Lindström, S., Sanei, H., Waajen, I., Fendley, I.M., Mather, T.A., Wang, Y., Rohovec, J., Navrátil, T., Sluijs, A., van de Schootbrugge, B., 2024. Climate-forced Hg-remobilization associated with fern mutagenesis in the aftermath of the end-Triassic extinction. Nat. Commun. 15 (1), 3596. https://doi.org/10.1038/s41467-024-47922-0.
- Brewer, P.G., Spencer, D.W., 1974. Distribution of some trace elements in Black Sea and their flux between dissolved and particulate phases. AAPG Bull. 145, 137–143.
- Canfield, D., Lyons, T., Raiswell, R., 1996. A model for iron deposition to euxinic Black Sea sediments. Am. J. Sci. 296, 818–834. https://doi.org/10.2475/ AIS 296 7.818
- Canfield, D., Raiswell, R., Westrich, J., Reaves, C., Berner, R., 1986. The use of chromium reduction in the analysis of reduced inorganic sulfur in sediments and shales. Chem. Geol. 54, 149–155. https://doi.org/10.1016/0009-2541(86) 90078-1.
- Carrillo, U., 2021. Impacts of volcanic eruptions and early recovery in freshwater environments and organisms. Biol. Rev. 96, 12766. https://doi.org/10.1111/brv.12766
- Cao, Y., Jin, Z., Zhu, R., Liu, K., Bai, J., 2024. Comprehensive evaluation of the organic-rich saline lacustrine shale in the Lucaogou Formation, Jimusar sag, Junggar Basin, NW China. Energy 294, 130786. https://doi.org/10.1016/j. energy.2024.130786.
- Chen, J., Chen, J., Shi, S., Yao, L., Chen, J., Khan, I., Zhang, C., 2020. The linkage of nitrogen isotopic composition and depositional environment of black mudstones in the Upper Triassic Yanchang Formation, Ordos Basin, northern China. J. Asian Earth Sci. 193, 104308. https://doi.org/10.1016/j.jseaes.2020.104308.
- Chen, Y., 2023. Phosphorus the main limiting factor in riverine ecosystems in China. Sci. Total Environ. 870, 161613. https://doi.org/10.1016/j.scitotenv.2023.161613.
- Chu, R., Wu, H., Zhu, R., Fang, Q., Deng, S., Cui, J., Yang, T., Li, H., Cao, L., Zhang, S., 2020. Orbital forcing of Triassic megamonsoon activity documented in lacustrine sediments from Ordos Basin, China. Palaeogeogr. Palaeoclimatol. Palaeoecol. 541, 109542. https://doi.org/10.1016/j.palaeo.2019.109542.
- Cleveland, W.S., 1979. Robust locally weighted regression and smoothing scatter-plots. J. Am. Stat. Assoc. 74, 829–836. https://doi.org/10.1080/01621459.1979.10481038.
- Cohen, K.M., Finney, S.C., Gibbard, P.L., Fan, J.X., 2013. The ICS international chronostratigraphic chart. Episodes 36, 199–204. https://doi.org/10.18814/epiiugs/2013/v36i3/002
- Dal Corso, J., Bernardi, M., Sun, Y., Song, H., Seyfullah, L.J., Preto, N., Gianolla, P., Ruffell, A., Kustatscher, E., Roghi, G., Merico, A., Hohn, S., Schmidt, A.R., Marzoli, A., Newton, R.J., Wignall, P.B., Benton, M.J., 2020. Extinction and dawn of the modern world in the Carnian (late Triassic). Sci. Adv. 6, eaba0099. https://doi.org/10.1126/sciadv.aba0099.
- Dong, Y., Liu, X., Zhang, G., Chen, Q., Zhang, X., Li, W., Yang, C., 2012. Triassic diorites and granitoids in the Foping area: constraints on the conversion from subduction to collision in the Qinling orogen, China. J. Asian Earth Sci. 47, 123–142. https://doi.org/10.1016/j.jseaes.2011.06.005.
- Fedo, C.M., Wayne Nesbitt, H., Young, G.M., 1995. Unraveling the effects of potassium metasomatism in sedimentary rocks and paleosols, with implications for paleoweathering conditions and provenance. Geology 23, 921. https://doi.org/10.1130/0091-7613(1995)023<0921:UTEOPM>2.3.CO;2.
- Galvez, M.E., Fischer, W.W., Jaccard, S.L., Eglinton, T.I., 2020. Materials and pathways of the organic carbon cycle through time. Nat. Geosci. 13, 535–546. https://doi.org/10.1038/s41561-020-0563-8.
- Gao, J., Jin, Z., Liang, X., Li, S., Yang, W., Zhu, R., Du, X., Liu, Q., Li, T., Dong, L., Li, P., Zhang, W., 2023. The impact of volcanism on eutrophication and water column in a freshwater lacustrine basin: A case study of Triassic Chang 7 Member in Ordos Basin. Oil Gas Geol. 44, 887–898. (in Chinese). https://doi.org/10.11743/ogg20230407.
- Gou, Q., Xu, S., 2023. The controls of laminae on lacustrine shale oil content in China: a review from generation, retention, and storage. Energies 16, 1987. https://doi.org/10.3390/en16041987.
- Hasegawa, T., 1997. Cenomanian-Turonian carbon isotope events recorded in terrestrial organic matter from northern Japan. Palaeogeogr. Palaeoclimatol. Palaeoecol. 130, 251–273. https://doi.org/10.1016/S0031-0182(96)00129-0.
- Ji, L., Yan, K., Meng, F., Zhao, M., 2010. The oleaginous botryococcus from the triassic Yanchang Formation in Ordos Basin, northwestern China: morphology and its paleoenvironmental significance. J. Asian Earth Sci. 38, 175–185. https:// doi.org/10.1016/j.jseaes.2009.12.010.

Jiang, M., Liu, Q., Wu, X., Zhu, D., 2025. Advancements in geochemistry and origins of CO₂ in natural gas reservoirs of China, Mar. Petrol. Geol. 173, 107267. https:// doi.org/10.1016/j.marpetgeo.2024.107267.

- Jin, C., Li, C., Algeo, T.J., Planavsky, N.J., Cui, H., Yang, X., Zhao, Y., Zhang, X., Xie, S., 2016. A highly redox-heterogeneous ocean in South China during the early Cambrian (-529-514 Ma): implications for biota-environment co-evolution. Earth. Planet. Sci. Lett. 441, 38-51. https://doi.org/10.1016/j.epsl.2016.02.019.
- Jin, Z., Wang, X., Wang, H., Ye, Y., Zhang, S., 2023. Organic carbon cycling and black shale deposition: an Earth System Science perspective. Natl. Sci. Rev. 10, nwad243. https://doi.org/10.1093/nsr/nwad243.
- Kiipli, T., Kallaste, T., Kiipli, E., Radzevičius, S., 2013. Correlation of silurian bentonites based on the immobile elements in the east baltic and scandinavia. GFF 135, 152–161. https://doi.org/10.1080/11035897.2013.783104.
- Landwehrs, J., Feulner, G., Willeit, M., Petri, S., Sames, B., Wagreich, M., Whiteside, J.
 H., Olsen, P.E., 2022. Modes of Pangean lake level cyclicity driven by astronomical climate pacing modulated by continental position and pCO2. Proc. Natl. Acad. Sci. U. S. A. 119, 46. https://doi.org/10.1073/pnas.2203818119.
 Laurin, J., Barclay, R.S., Sageman, B.B., Dawson, R.R., Pagani, M., Schmitz, M.,
- Laurin, J., Barclay, R.S., Sageman, B.B., Dawson, R.R., Pagani, M., Schmitz, M., Eaton, J., McInerney, F.A., McElwain, J.C., 2019. Terrestrial and marginal-marine record of the mid-Cretaceous Oceanic Anoxic Event 2 (OAE 2): high-resolution framework, carbon isotopes, CO₂ and sea-level change. Palaeogeogr. Palaeoclimatol. Palaeoecol. 524, 118–136. https://doi.org/10.1016/j.palaeo.2019.03.019.
- Lewis, B.L., Landing, W.M., 1991. The biogeochemistry of manganese and iron in the Black Sea. Deep-Sea Res. Part A Oceanogr. Res. Pap. 38, S773–S803. https://doi.org/10.1016/S0198-0149(10)80009-3.
- Li, M., Hinnov, L., Kump, L., 2019. Acycle: time-series analysis software for paleoclimate research and education. Comput. Geosci. 127, 12–22. https://doi.org/ 10.1016/j.cageo.2019.02.011.
- Li, M., Kump, L.R., Hinnov, L.A., Mann, M.E., 2018. Tracking variable sedimentation rates and astronomical forcing in Phanerozoic paleoclimate proxy series with evolutionary correlation coefficients and hypothesis testing. Earth Planet Sci. Lett. 501, 165–179. https://doi.org/10.1016/j.epsl.2018.08.041.
- Li, Q., Wu, S., Xia, D., You, X., Zhang, H., Lu, H., 2020. Major and trace element geochemistry of the lacustrine organic-rich shales from the Upper Triassic Chang 7 Member in the southwestern Ordos Basin, China: implications for paleoenvironment and organic matter accumulation. Mar. Petrol. Geol. 111, 852–867. https://doi.org/10.1016/j.marpetgeo.2019.09.003.
- Li, Z., Zhang, Y., Torres, M., Mills, B.J.W., 2023. Neogene burial of organic carbon in the global ocean. Nature 613, 90–95. https://doi.org/10.1038/s41586-022-05413-6
- Liang, X., Jin, Z., Liu, Q., Alexander, S., Li, P., Vladimir, M., Boris, U., 2021. Impact of volcanic ash on the formation of organic-rich shale: a case study on the Mesozoic Bazhenov Formation, West Siberian Basin. Oil Gas Geol. 42, 201–211. (in Chinese). https://doi.org/10.11743/ogg20210117.
- Lin, S., Hou, L., Luo, X., Wu, Y., 2022. A millimeter-scale insight into formation mechanism of lacustrine black shale in tephra deposition background. Sci. Rep. 12, 11511. https://doi.org/10.1038/s41598-022-15715-4.
- Little, S., Vance, D., Lyons, T., McManus, J., 2015. Controls on trace metal authigenic enrichment in reducing sediments: insights from modern oxygen-deficient settings. Am. J. Sci. 315, 77–119. https://doi.org/10.2475/02.2015.01.
- Liu, D., 2021. Paleoclimate and sea level response to orbital forcing in the Middle Triassic of the eastern Tethys. Global Planet. Change 199, 103454. https://doi. org/10.1016/j.gloplacha.2021.103454.
- Liu, Q., Li, P., Jiang, L., Jin, Z., Liang, X., Zhu, D., Pang, Q., Zhang, R., Liu, J., 2024. Distinctive volcanic ash–rich lacustrine shale deposition related to chemical weathering intensity during the Late Triassic: evidence from lithium contents and isotopes. Sci. Adv. 10, 6594. https://doi.org/10.1126/sciadv.adi6594.
- Liu, Q., Li, P., Jin, Z., Liang, X., Zhu, D., Wu, X., Meng, Q., Liu, J., Fu, Q., Zhao, J., 2021. Preservation of organic matter in shale linked to bacterial sulfate reduction (BSR) and volcanic activity under marine and lacustrine depositional environments. Mar. Petrol. Geol. 127, 104950. https://doi.org/10.1016/j.marpetgeo.2021.104950.
- Liu, Q., Li, P., Jin, Z., Sun, Y., Hu, G., Zhu, D., Huang, Z., Liang, X., Zhang, R., Liu, J., 2022. Organic rich formation and hydrocarbon enrichment in lacustrine shale rock formations: a case study of Chang 7. Chin. Sci. Earth. Sci. 52, 270–290. https://doi.org/10.1007/s11430-021-9819-y.
- Lu, J., Zhang, P., Dal Corso, J., Yang, M., Wignall, P.B., Greene, S.E., Shao, L., Lyu, D., Hilton, J., 2021. Volcanically driven lacustrine ecosystem changes during the Carnian Pluvial Episode (late Triassic). Proc. Natl. Acad. Sci. 118, e2109895118. https://doi.org/10.1073/pnas.2109895118.
- Lu, J., Zhang, P., Yang, M., Shao, L., Hilton, J., 2020. Continental records of organic carbon isotopic composition (δ^{13} Corg), weathering, paleoclimate and wildfire linked to the End-Permian Mass Extinction. Chem. Geol. 558, 119764. https://doi.org/10.1016/j.chemgeo.2020.119764.
- Lu, Y., Hao, F., Yan, D., Lu, Y., 2021. Volcanism-induced late Boda warming in the Late Ordovician: Evidence from the Upper Yangtze Platform, South China. Palaeogeogr. Palaeoclimatol. Palaeoecol. 578, 110579. https://doi.org/10.1016/j. palaeo.2021.110579.
- Lu, Y., Jiang, S., Lu, Y., Xu, S., Shu, Y., Wang, Y., 2019. Productivity or preservation? The factors controlling the organic matter accumulation in the late Katian through Hirnantian Wufeng organic-rich shale, South China. Mar. Petrol. Geol. 109, 22–35. https://doi.org/10.1016/j.marpetgeo.2019.06.007.
- Mclennan, S.M., 1993. Weathering and global denudation. J. Geol. 101, 295–303. https://doi.org/10.1086/648222.

McLennan, S.M., Taylor, S.R., 1991. Sedimentary rocks and crustal evolution: tectonic setting and secular trends. J. Geol. 99, 1–21. https://doi.org/10.1086/620470

- Montero-Serrano, J.C., Föllmi, K.B., Adatte, T., Spangenberg, J.E., Tribovillard, N., Fantasia, A., Suan, G., 2015. Continental weathering and redox conditions during the early toarcian oceanic anoxic event in the northwestern Tethys: insight from the posidonia shale section in the Swiss jura Mountains. Palaeogeogr. Palaeoclimatol. Palaeoecol. 429, 83–99. https://doi.org/10.1016/j.palaeo.2015.03.043.
- Nesbitt, H.W., Young, G.M., 1982. Early Proterozoic climates and plate motions inferred from major element chemistry of lutites. Nature 299, 715–717. https:// doi.org/10.1038/299715a0.
- Owens, J.D., Lyons, T.W., Lowery, C.M., 2018. Quantifying the missing sink for global organic carbon burial during a Cretaceous oceanic anoxic event. Earth Planet Sci. Lett. 499, 83–94, https://doi.org/10.1016/j.epsl.2018.07.021.
- Panahi, A., Young, G.M., Rainbird, R.H., 2000. Behavior of major and trace elements (including REE) during Paleoproterozoic pedogenesis and diagenetic alteration of an Archean granite near Ville Marie, Québec, Canada. Geochem. Cosmochim. Acta 64, 2199–2220. https://doi.org/10.1016/S0016-7037(99)00420-2.
- Poulton, S., Canfield, D., 2011. Ferruginous conditions: a dominant feature of the ocean through earth's history. Elements 7, 107–112. https://doi.org/10.2113/GSELEMENTS.7.2.107.
- Poulton, S., Canfield, D., 2005. Development of a sequential extraction procedure for iron: implications for iron partitioning in continentally derived particulates. Chem. Geol. 214, 209–221. https://doi.org/10.1016/J.CHEMGEO.2004.09.003.
- Poulton, S.W., 2021. The Iron Speciation Paleoredox Proxy: Elements in Geochemical Tracers in Earth System Science. Camb. Univ. Press, p. 24. https://doi.org/10.1017/9781108847148.
- Raiswell, R., Canfield, D., 2012. The iron biogeochemical cycle past and present. Geochem. Perspect. 1, 1–2. https://doi.org/10.7185/GEOCHEMPERSP.1.1.
- Raiswell, R., Hardisty, D., Lyons, T., Canfield, D., Owens, J., Planavsky, N., Poulton, S., Reinhard, C., 2018. The iron paleoredox proxies: a guide to the pitfalls, problems and proper practice. Am. J. Sci. 318, 491–526. https://doi.org/10.2475/ 05.2018.03
- Schoepfer, S.D., Shen, J., Wei, H., Tyson, R.V., Ingall, E., Algeo, T.J., 2015. Total organic carbon, organic phosphorus, and biogenic barium fluxes as proxies for paleomarine productivity. Earth Sci. Rev. 149, 23–52. https://doi.org/10.1016/j. earscirev.2014.08.017.
- Scotese, C.R., Song, H., Mills, B.J.W., Van Der Meer, D.G., 2021. Phanerozoic paleotemperatures: the earth's changing climate during the last 540 million years. Earth Sci. Rev. 215, 103503. https://doi.org/10.1016/j.earscirev.2021.103503.
- Slomp, C.P., Thomson, J., De Lange, G.J., 2004. Controls on phosphorus regeneration and burial during formation of eastern Mediterranean sapropels. Mar. Geol. 203, 141–159. https://doi.org/10.1016/S0025-3227(03)00335-9.
- Sun, Y., Li, X., Liu, Q., Zhang, M., Li, P., Zhang, R., Shi, X., 2020. In search of the inland carnian pluvial event: middle-upper triassic transition profile and U-Pb isotopic dating in the Yanchang Formation in Ordos Basin, China. Geol. J. 55, 4905–4919. https://doi.org/10.1002/gj.3691.
- Tissot, B., Welte, D., 1984. Petroleum Formation and Occurrence. Springer, Verlag Berlin Heidelberg. https://link.springer.com/book/10.1007/978-3-642-96446-6.
- Tomimatsu, Y., Nozaki, T., Sato, H., Takaya, Y., Kimura, J.I., Chang, Q., Naraoka, H., Rigo, M., Onoue, T., 2021. Marine osmium isotope record during the Carnian "pluvial episode" (Late Triassic) in the pelagic Panthalassa Ocean. Global Planet. Change 197, 103387. https://doi.org/10.1016/j.gloplacha.2020.103387.
- Tribovillard, N., Algeo, T.J., Baudin, F., Riboulleau, A., 2012. Analysis of marine environmental conditions based onmolybdenum-uranium covariation—applications to Mesozoic paleoceanography. Chem. Geol. 324–325, 46–58. https://doi.org/10.1016/j.chemgeo.2011.09.009.
- Tribovillard, N., Algeo, T.J., Lyons, T., Riboulleau, A., 2006. Trace metals as paleoredox and paleoproductivity proxies: an update. Chem. Geol. 232, 12–32. https://doi.org/10.1016/j.chemgeo.2006.02.012.
- Trotter, J.A., Williams, I.S., Nicora, A., Mazza, M., Rigo, M., 2015. Long-term cycles of Triassic climate change: a new δ¹⁸O record from conodont apatite. Earth Planet Sci. Lett. 415, 165–174. https://doi.org/10.1016/j.epsl.2015.01.038.
- Vink, S., Chambers, R.M., Smith, S.V., 1997. Distribution of phosphorus in sediments from tomales bay, California. Mar. Geol. 139, 157–179. https://doi.org/10.1016/ S0025-3227(96)00109-0.
- Walton, C.R., Ewens, S., Coates, J.D., Blake, R.E., Planavsky, N.J., Reinhard, C., Ju, P., Hao, J., Pasek, M.A., 2023. Phosphorus availability on the early Earth and the impacts of life. Nat. Geosci. 16, 399–409. https://doi.org/10.1038/s41561-023-01167.6
- Wang, M., Chen, H., Huang, C., Kemp, D.B., Xu, T., Zhang, H., Li, M., 2020. Astronomical forcing and sedimentary noise modeling of lake-level changes in the Paleogene Dongpu Depression of North China. Earth Planet Sci. Lett. 535, 116116. https://doi.org/10.1016/j.epsl.2020.116116.
- Wang, X., Dong, L., Li, T., Ling, K., Zhang, C., Bin, Y., Wang, Z., Jin, Z., Fu, J., 2024. Reconstructing redox landscape with coupled nitrogen-sulfur isotopes: a case study from middle-late triassic Chang 7 member of the Yanchang Formation in the Ordos Basin (North China). Geochem. Geophys. Geosystems 25, e2024GC011656. https://doi.org/10.1029/2024GC011656.
- Wang, X., Wang, T., Zhang, C., 2013. Neoproterozoic, paleozoic, and mesozoic granitoid magmatism in the Qinling Orogen, China: constraints on orogenic process. J. Asian Earth Sci. 72, 129–151. https://doi.org/10.1016/j. jseaes.2012.11.037.

- Wang, X., Zhang, S., Ye, Y., Ma, S., Su, J., Wang, H., Canfield, D.E., 2023. Nitrogen cycling during the mesoproterozoic as informed by the 1400 million year old Xiamaling Formation. Earth Sci. Rev. 243, 104499. https://doi.org/10.1016/j.earscirev.2023.104499.
- Wei, R., Zhang, R., Li, M., Wang, X., Jin, Z., 2023. Obliquity forcing of lake-level changes and organic carbon burial during the Late Paleozoic Ice Age. Global Planet. Change 223, 104092. https://doi.org/10.1016/j.gloplacha.2023.104092.
- Wu, X., Luo, H., Zhang, J., Chen, Q., Fang, X., Wang, W., Li, W., Shi, Z., Zhang, Y., 2023. Volcanism-driven marine eutrophication in the end-Ordovician: evidence from radiolarians and trace elements of black shale in South China. J. Asian Earth Sci. 253, 105687. https://doi.org/10.1016/j.jseaes.2023.105687.
- Yang, J., Cawood, P.A., Condon, D.J., Liu, J., Deng, X., Wang, J., Du, Y., Yuan, D., 2022. Anomalous weathering trends indicate accelerated erosion of tropical basaltic landscapes during the Permo-Triassic warming. Earth Planet Sci. Lett. 577, 117256. https://doi.org/10.1016/j.epsl.2021.117256.
- Yang, S., Hu, W., Fan, J., Deng, Y., 2022. New geochemical identification fingerprints of volcanism during the Ordovician-Silurian transition and its implications for biological and environmental evolution. Earth Sci. Rev. 228, 104016. https:// doi.org/10.1016/j.earscirev.2022.104016
- Yang, S., Hu, W., Wang, X., Jiang, B., Yao, S., Sun, F., Huang, Z., Zhu, F., 2019. Duration, evolution, and implications of volcanic activity across the Ordovician–Silurian transition in the Lower Yangtze Region, South China. Earth Planet Sci. Lett. 518, 13–25. https://doi.org/10.1016/j.epsl.2019.04.020.
- Yang, Y., Li, W., Ma, L., 2005. Tectonic and stratigraphic controls of hydrocarbon systems in the Ordos Basin: a multicycle cratonic basin in central China. AAPG Bull. 89, 255–269. https://doi.org/10.1306/10070404027.
- Yin, H., Wei, W., Jing, Z., Zou, C., Xu, W., Hao, J., Huang, F., 2024. Cd isotope evidence for elevated productivity in the Middle Triassic Ordos Basin. Geochem. Perspect. Lett. 33, 13–19. https://doi.org/10.7185/geochemlet.2446.

- Yuan, W., Chen, R., Liu, G., Shang, F., Xu, L., Niu, X., 2019. Linking the Qinling Orogeny with the Chang 7 shale (Triassic Yanchang Formation) deposition: evidence from major, trace, and rare earth element geochemistry. Geol. J. 54, 133–142. https://doi.org/10.1002/gj.3164.
- Yuan, W., Liu, G., Bulseco, A., Zhou, X., 2021. Iron speciation in organic-rich shales from the upper triassic Yanchang Formation, Ordos Basin, Northern China: implications for depositional environment. J. Asian Earth Sci. 220, 104917. https://doi.org/10.1016/j.jseaes.2021.104917.
- Yuan, W., Liu, G., Zhou, X., Bulseco, A., 2022. Linking hydrothermal activity with organic matter accumulation in the Chang 7 black shale of Yanchang Formation, Ordos Basin, China. Front. Earth Sci. 10, 786634. https://doi.org/10.3389/ feart.2022.786634.
- Zhang, W., Yang, H., Peng, P., Yang, Y., Zhang, H., Shi, X., 2009. The influence of Late Triassic volcanic activity on the development of high-quality source rocks of Chang 7 in the Ordos Basin. Geochimica 38, 573–582. https://doi.org/10.19700/ i.0379-1726.2009.06.007.
- Zhang, W., Yang, W., Xie, L., 2017. Controls on organic matter accumulation in the Triassic Chang 7 lacustrine shale of the Ordos Basin, central China. Int. J. Coal Geol. 183, 38–51. https://doi.org/10.1016/j.coal.2017.09.015.
- Zhao, W., Wang, X., Hu, S., Zhang, S., Wang, H., Guan, S., Ye, Y., Ren, R., Wang, T., 2019. Hydrocarbon generation characteristics and exploration prospects of Proterozoic source rocks in China. Sci. China Earth Sci. 62, 909–934. https://doi.org/10.1007/s11430-018-9312-4.
- Zhu, R., Cui, J., Deng, S., Luo, Z., Lu, Y., Qiu, Z., 2019. High-precision dating and geological significance of Chang 7 tuff zircon of the triassic Yanchang Formation, Ordos Basin in Central China. Acta Geol. Sin. - Engl. Ed. 93, 1823–1834. https://doi.org/10.1111/1755-6724.14329.